Article

Double-Confined Ultrafine Cobalt Clusters for Efficient Peroxide Activation

Xiaowen Xie, Mingshan Zhu, Fei Xiao, Yongjie Xiang, Huanran Zhong, Zhimin Ao, and Haibao Huang*

Cite This: JACS Au 2023, 3, 1496−1506

Read Online

ACCESS | Metrics & More | Article Recommendations | Supporting Information

ABSTRACT: The construction of highly active catalysts presents great prospects, while it is a challenge for peroxide activation in advanced oxidation processes (AOPs). Herein, we facilely developed ultrafine Co clusters confined in mesoporous silica nanospheres containing N-doped carbon (NC) dots (termed as $Co/NC@mSiO_2$) via a double-confinement strategy. Compared with the unconfined counterpart, $Co/NC@mSiO_2$ exhibited unprecedented catalytic activity and durability for removal of various organic pollutants even in extremely acidic and alkaline environments (pH from 2 to 11) with very low Co ion leaching. Experiments and density functional theory (DFT) calculations proved that $Co/NC@mSiO_2$ possessed strong peroxymonosulphate (PMS) adsorption and charge transfer capability, enabling the efficient O−O bond dissociation of PMS to $HO^\bullet$ and $SO_4^{\bullet-}$ radicals. The strong interaction between Co clusters and $mSiO_2$ containing NC dots contributed to excellent pollutant degradation performances by optimizing the electronic structures of Co clusters. This work represents a fundamental breakthrough in the design and understanding of the double-confined catalysts for peroxide activation.

KEYWORDS: AOPs, double confinement, strong metal−support interaction, cobalt clusters, electron transfer
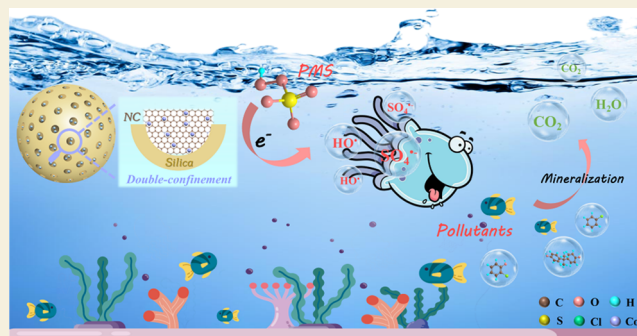
INTRODUCTION

Billions of tons of organic chemicals are discharged into the environment from various industries, posing huge risks to ecosystems and human health. Peroxide activation has been extensively used in many fields over the past decades, especially in environmental remediation.[1−3] Heterogeneous transition-metal catalysts can activate the peroxide bond for in situ generation of powerful reactive oxygen species (ROS) to degrade organic pollutants and have attracted increasing interest due to their advantages of high abundance and low price. However, the well-explored heterogeneous metal catalysts such as Co_3O_4,[4] $CoFe_2O_4$,[5] CuO,[6] and MnO_2[7] were mainly in the form of aggregated particles with low metal dispersion and atomic utilization. Heterogeneous peroxide activation is therefore severely hampered by the poor activity and stability of catalysts due to metal aggregation, leakage, and poisoning under complicated conditions.[8] Recently, nano-particles (NPs), clusters, or even single-atom catalysts have been widely developed to improve active site exposure and atom utilization.[9,10] Compared with those heterogeneous materials, they not only possess homogenized active species for catalytic reactions, which are similar to homogeneous materials, but also have extra advantages of high reusability and durability derived from heterogeneous materials.[11] Never-theless, significant challenges related to the synthesis and stabilization of these highly dispersed catalysts exist in their application. It is difficult to stabilize isolated metals or clusters on supports without the compromise of catalytic activity, especially at high temperatures or under harsh reaction conditions.[12] Therefore, there is an urgent need to develop highly active and stable metal catalysts for their applications in real environments.

It has been reported that the physical confinement of metal NPs, clusters, or single atoms inside porous materials can greatly enhance the catalytic activity.[13,14] Compared with the bulk catalysts, the confined catalysts exhibit superior metastable polymorph stability, nucleation probability, metal dispersion, and thermal stability,[8] which is beneficial to enhance the reactivity and avoid catalytic deactivation in advanced oxidation processes (AOPs). The most widely studied physical confinement of porous materials such as zeolite,[15] SiO_2,[16] and carbon[17] can suppress metal aggregation, while it is still difficult to disperse the metal atoms into a
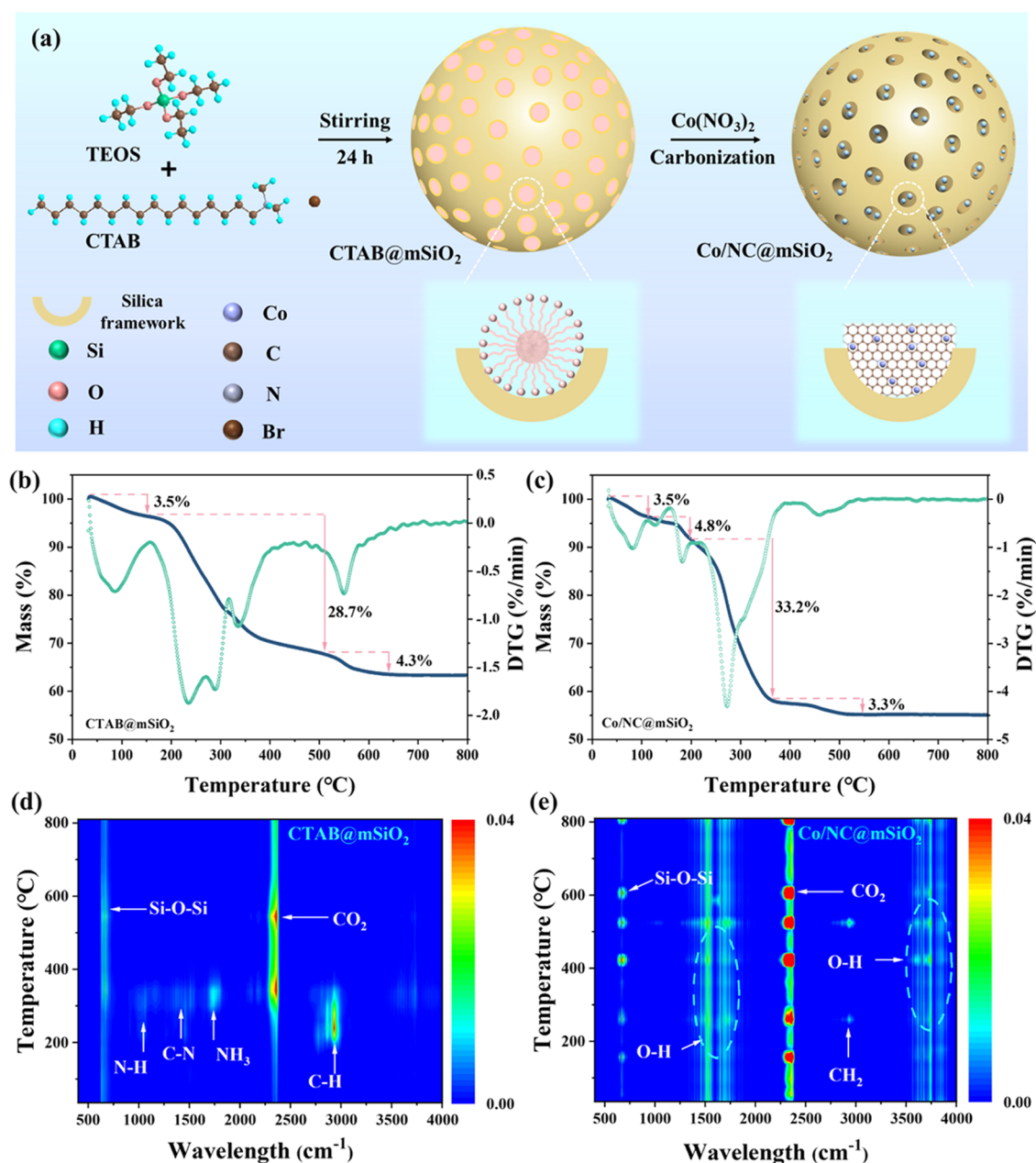
Figure 1. Formation procedure of Co/NC@mSiO$_2$ (a). Thermogravimetric analysis (TGA) and derivative thermogravimetry (DTG) curves of CTAB@mSiO$_2$ (b) and Co/NC@mSiO$_2$ (c). In situ Fourier transform infrared (FTIR) profiles of the gas products released from CTAB@mSiO$_2$ (d) and Co/NC@mSiO$_2$ (e).

cluster or single-atom level. Recently, the strong metal–support interaction (SMSI) has been found to effectively regulate the metal electronic structure and stabilize metals via chemical confinement, thus further improving metal dispersion and catalytic activity.[18] The defective nitrogen-doping carbon (NC) or functional groups have been reported to well confine the active sites due to the SMSI effect.[19] Nano-mesoporous silica spheres (mSiO$_2$) can well disperse the metal atoms mainly via physical confinement due to the abundant mesoporous channels, high specific surface area, and thermodynamic stability.[20,21] Nitrogen-containing surfactants such as cetyltrimethylammonium bromide (CTAB) are generally used as templates in the synthesis of mSiO$_2$,[22] which will generate numerous gas pollutants during their high-temperature removal. Recent studies found that CTAB can be

used as promising precursors to prepare NC dots via the carbonization process.[23,24] The repulsive force between the metal particles is greater than the van der Waals force due to the increased CTAB molecules near the metal particles. In this case, the NPs would gradually change from agglomeration to monodispersion.[25] This further inspires us to directly obtain NC dots by utilizing CTAB carbonization to further enhance metal dispersion via the double confinement during the synthesis of mSiO$_2$.

Herein, we originally developed the ultrafine Co clusters confined in mSiO$_2$ nanospheres containing NC dots (termed as Co/NC@mSiO$_2$) by a facile solvent-free method. The physical confinement effect of mSiO$_2$ mesopores prevented the migration of Co clusters between layers. Meanwhile, the SMSI between Co clusters and mSiO$_2$ containing NC dots improved
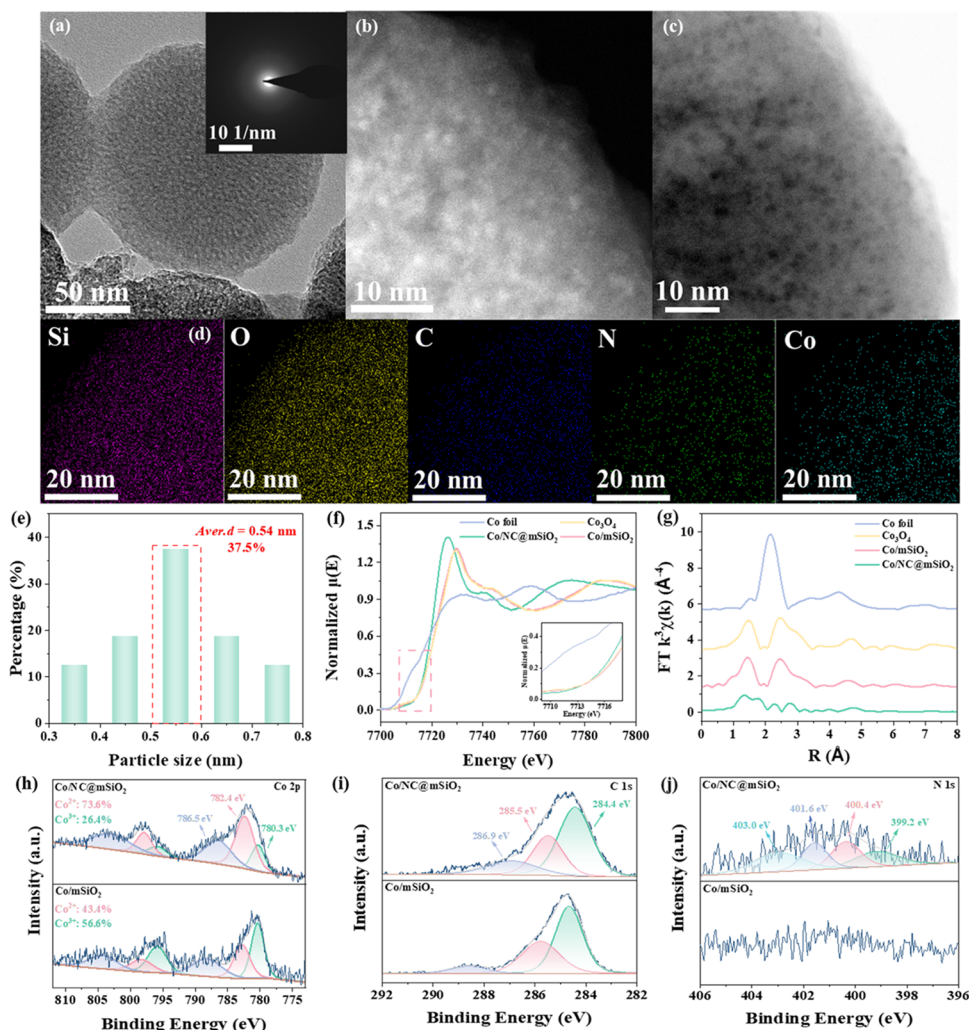
Figure 2. HRTEM (a), aberration-corrected HAADF-STEM (b), HAABF-STEM (c), and EDS elemental mapping images (d) of Co/NC@mSiO$_2$. Histogram of Co cluster diameter distribution (e). Normalized Co K-edge X-ray absorption near-edge structure (XANES) spectra of Co foil and Co-based samples (f). Corresponding extended X-ray absorption fine structure (EXAFS) fitting curves of Co foil and Co-based samples at the R space (g). X-ray photoelectron spectroscopy (XPS) of Co 2p (h), C 1s (i), and N 1s (j) spectra of Co-based catalysts.

the electron transport properties of Co/NC@mSiO$_2$ through the chemical confinement. The double physical−chemical confinement strategy worked well to prevent metal aggregation during calcination. Co/NC@mSiO$_2$ exhibited exceptional catalytic activity and stability toward peroxymonosulfate (PMS, one of the peroxides) activation for efficient degradation of various organic pollutants even under harsh conditions. The SMSI effect between Co clusters and mSiO$_2$ containing NC dots achieved excellent pollutant degradation performances by optimizing the electronic structures of Co clusters. Co/NC@mSiO$_2$ possessed strong PMS adsorption and charge transfer capability, achieving the efficient PMS activation into reactive radicals. This study provides a novel double-confinement strategy for the design of highly active and stable nanocatalyst and insight into mechanisms of peroxide activation during environmental remediation.

RESULTS AND DISCUSSION

Synthesis and Characterization of the Catalyst

The double-confined Co/NC@mSiO$_2$ was fabricated by a facile and green solvent-free method (Figure 1a). In detail, Co(NO$_3$)$_2$·6H$_2$O and the spherical CTAB@mSiO$_2$ were used as the metal precursor and support, respectively. Notably, CTAB@mSiO$_2$ was prepared via the sol−gel method without removing CTAB templates (Figure S1), which can provide abundant silicon hydroxyl (Si−OH) as the anchoring sites, as well as an extraordinary confined space between the template and silica walls to limit the growth of metal species. The decomposition of the Co precursor proceeded within the confined space between the template and silica frameworks. After high-temperature carbonization, the highly dispersed Co clusters were successfully confined in mSiO$_2$ mesopores containing NC dots. For comparison, Co/mSiO$_2$ was also synthesized using a similar method but with spherical mSiO$_2$ (after removal of CTAB templates, Figure S2) as the support.

The key effect of CTAB carbonization on the formation of the double-confined Co/NC@mSiO$_2$ catalyst was first explored. The in situ TG-FTIR test was conducted under an air atmosphere to study the transformation process of the presynthesized samples during calcination. As seen in Figure 1b,c, all samples showed an initial mass loss in the DTG curve at 30−110 °C due to the loss of physically adsorbed water.[26] The CTAB@mSiO$_2$ displayed a weight loss of 28.7% at 150− 500 °C, corresponding to the CTAB decomposition.[25] As the

temperature further increased, a slow decrease in weight (4.3%) at 500−650 °C derived from the decomposition of NC dots in $mSiO_2$.[23] As for the presynthesized $Co/NC@mSiO_2$, about 4.8% of weight loss was observed from 100 to 200 °C with a DTG peak at 180 °C corresponding to the decomposition of $Co(NO_3)_2 \cdot 6H_2O$.[27] However, the $mSiO_2$ and presynthesized $Co/mSiO_2$ did not show any DTG peaks attributed to CTAB decomposition, illustrating that the CTAB micelles had been completely removed after calcination (Figure S3). The in situ FTIR test was used to examine the gaseous products evolved at different temperatures in the process of catalyst synthesis (Figure 1d−e). For CTAB@ $mSiO_2$, the strong absorptions at 2936 $cm^{−1}$ were caused by the C−H stretching vibration of methyl and methylene groups of CTAB in the range of 200−300 °C.[28] The small bands observed at 1751, 1470, and 1129 $cm^{−1}$ can be attributed to the NH_3, C−N stretching, and N−H bending, respectively. Interestingly, the presynthesized $Co/NC@mSiO_2$ displayed much higher CO_2 yields than CTAB@$mSiO_2$, and no obvious toxic gas pollutants were generated, indicating that the preparation process of $Co/NC@mSiO_2$ was environmentally friendly. On the other hand, Co clusters can catalyze CTAB decomposition to generate abundant CO_2 during the heating process, resulting in the formation of richer mesoporous structures. This, in turn, favored the diffusion of Co clusters in the pore channels. The in situ TG-FTIR results demonstrated that NC dots were successfully formed from the carbonization of CTAB in $mSiO_2$ nanospheres.

Various characterizations were then conducted to explore the morphologies and structures of the prepared catalysts. The X-ray diffraction (XRD) patterns of all samples showed a typical wide diffraction peak at 23°, representing the characteristic reflection of a uniform mesostructure (Figure S4). Surprisingly, no diffraction peaks of Co species can be observed over $Co/NC@mSiO_2$, indicating its exceptional dispersion and ultrafine size. However, $Co/mSiO_2$ exhibited several diffraction peaks at 31.2, 36.9, 44.7, 59.1, and 65.3° assigned to Co_3O_4 NPs with an average size of 17.0 nm (calculated by the Scherrer equation).[4] Further, the large Co_3O_4 NPs marked with yellow circles can also be clearly found on the external surface of $Co/mSiO_2$ (Figure S5). Both of these strongly verified the formation of Co NPs rather than clusters on the pure $mSiO_2$ supports without the existence of CTAB templates. Compared with $Co/mSiO_2$, $Co/NC@mSiO_2$ showed a larger S_{BET} of 1293 m^2 $g^{−1}$ but a smaller pore volume (0.68 cm^3 $g^{−1}$), which may be attributed to the incorporation of Co species into mesopores of $mSiO_2$ (Figure S6 and Table S1). The corresponding pore-size distribution indicated the presence of abundant mesopores with an average diameter of 5.0 nm. The large surface of $Co/NC@mSiO_2$ helped to facilitate the metal active site dispersion and reactant adsorption, while its small pore volume could enhance the interaction between reactants and Co clusters.

The high dispersion of Co species was further proved by the results of scanning electron microscopy (SEM) (Figure S7) and high-resolution transmission electron microscopy (HRTEM) (Figure 2a). No obvious Co NPs were observed on their external surface, suggesting that Co species was confined in the mesopores of the nanospheres via the physical confinement effect. The aberration-corrected high-angle annular dark-field and bright-field scanning TEM (HAADF/ HAABF-STEM) were performed to disclose the distribution of Co species over $Co/NC@mSiO_2$ (Figure 2b,c). Numerous

bright/black dots encapsulated in the mesopores can be clearly observed in different domains of the $mSiO_2$ nanospheres. The scanning transmission electron microscopy−energy-dispersive X-ray spectroscopy (STEM-EDS) elemental mapping of Co/ $NC@mSiO_2$ exhibited a uniform distribution of Si, O, C, N, and Co elements (Figure 2d), with the C and N contents of 13.39 and 0.21 wt % determined by quantitative element analysis, respectively (Table S2). The average diameter of these black dots was measured to be only ∼0.54 nm (Figure 2e), demonstrating that the well-confined Co species mainly existed in the form of ultrafine clusters via the physical confinement effect.

X-ray absorption near-edge structure (XANES) and extended X-ray absorption fine structure (EXAFS) spectroscopies were performed to study the coordination state of Co clusters. As shown in Figure 2f, the absorption edge position of Co element in $Co/NC@mSiO_2$ was located between Co foil and Co_3O_4, demonstrating that the valence of Co was higher than that of the metallic Co but lower than that of Co^{3+} (named as $Co^{\delta+}$, $0 < \delta < 3$).[29] The Fourier transform (FT) k^3-weighted EXAFS (FT-EXAFS) spectrum showed the main peak at ∼1.30 Å, which can be assigned to the scattering interaction between Co and N/O in the first-shell CoN(O) (Figure 2g). In addition, another peak at ∼1.80 Å can be attributed to Co−Br coordination. The structural parameters were further extracted (Table S3). The coordination numbers for N and Br were calculated to be 4.9 and 2.2 with the average bond lengths of 1.92 and 2.26 Å, respectively. The existence of Co−N and Co−Br bonds proved evidence for the chemical confinement of NC dots for the formation of Co clusters. In addition, there also existed coordination peaks of Co−Co (∼2.30 Å) and Co−O (∼2.80 Å) bonds, suggesting the presence of Co clusters in $Co/NC@mSiO_2$. As for $Co/mSiO_2$, it showed similar coordination and state with the Co_3O_4 sample. It was thus reasonable to infer that the formation of NC dots from CTAB carbonization significantly changed the coordination and state of Co clusters in $Co/NC@mSiO_2$.

The XPS analysis was further performed to confirm the chemical state of Co element in Co-based catalysts. Si, O, C, and Co elements can be easily detected in the full XPS spectrum of both samples, while the peak assigned to N element was not obvious due to its low content (Figure S8). In detail, an obvious peak between Co^{3+} (780.3 eV) and Co^{2+} (782.4 eV) was observed in the Co 2p fine spectrum of Co/ $NC@mSiO_2$ (Figure 2h), in accordance with the above XANES results. Significantly, compared with $Co/mSiO_2$, the Co 2p peaks of $Co/NC@mSiO_2$ clearly shifted, indicating the stronger electron binding energy. This could be ascribed to varying degrees of the reaction between Co clusters and $mSiO_2$ containing NC dots at the interface, giving rise to the formation of Co−N/Br or Co−O−Si bonds. Additionally, the high Co^{2+} ratio of 73.6% (Tables S4 and S5) in Co/NC@ $mSiO_2$ proved that the SMSI effect between Co clusters and $mSiO_2$ containing NC dots optimized the electronic structures[23] and prevented the surface oxidation of Co clusters. The high-resolution C 1s spectrum of $Co/NC@mSiO_2$ exhibited three peaks assigned to C═C (284.4 eV), C−O− C (285.5 eV), and C═O (286.9 eV),[29] respectively (Figure 2i). Among them, the higher proportion of C═C groups (54.7%) in $Co/NC@mSiO_2$ reflected its high degree of graphitization, which was conducive to promote charge transfer. Compared with $Co/NC@mSiO_2$, the C 1s spectrum of $Co/mSiO_2$ obviously shifted toward a higher binding energy
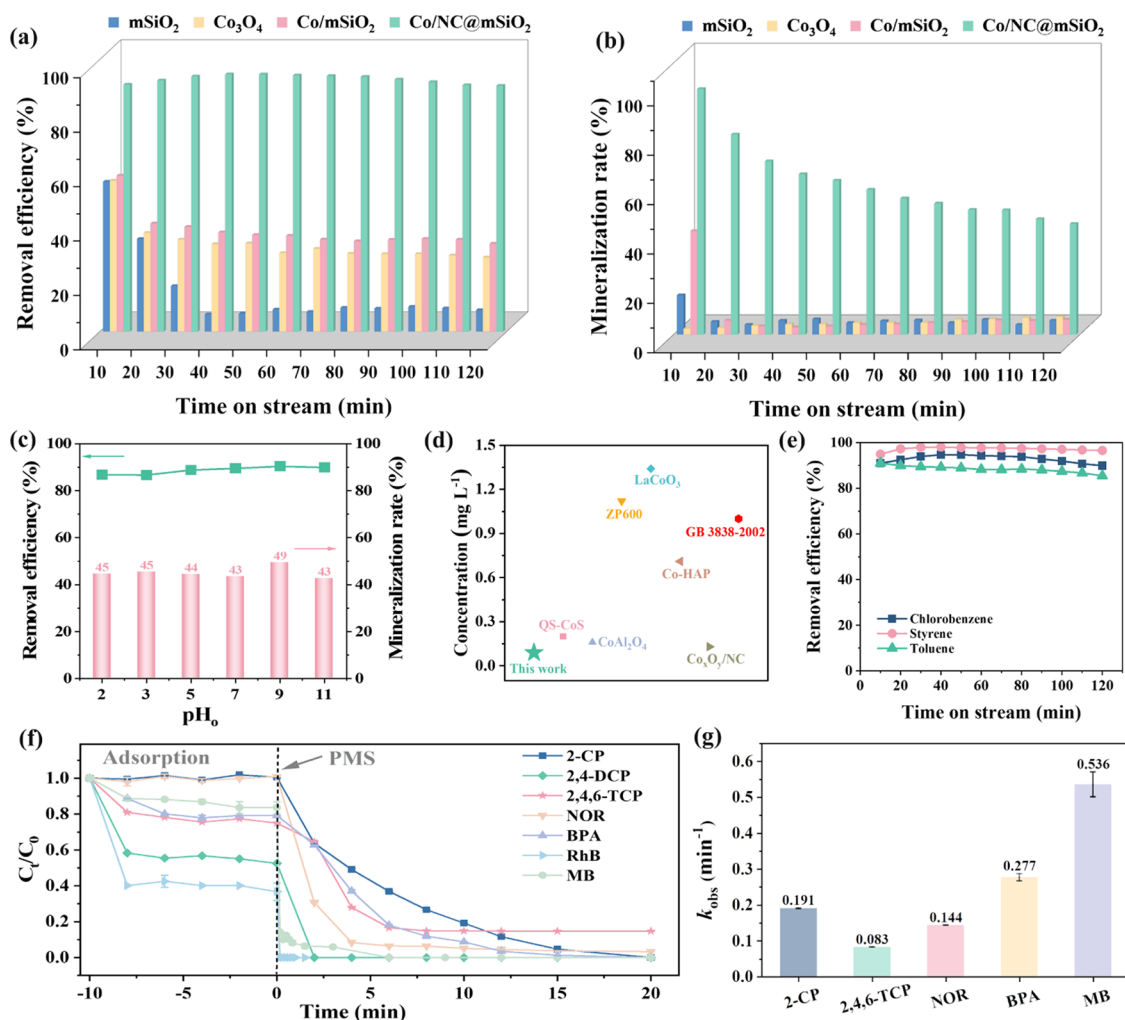
Figure 3. Chlorobenzene degradation over different catalysts at initial pH 7 (a, b). Chlorobenzene degradation over Co/NC@mSiO$_2$ at different pH values (c). The leaching concentration of Co ions in the Co/NC@mSiO$_2$/PMS system and other works (d). Degradation of different gaseous VOCs over Co/NC@mSiO$_2$ (e). Degradation of different organic pollutants in wastewater over Co/NC@mSiO$_2$ (f, g). ([VOCs]$_o$ = 30 ppmv, [Catalyst]$_o$ = 50 mg L^{-1}, [PMS]$_o$ = 16 mM, T = 25 °C; [Organic pollutant in wastewater]$_o$ = 10 mg L^{-1}, [Catalyst]$_o$ = 10 mg L^{-1}, [PMS]$_o$ = 0.32 mM, T = 25 °C).

and did not show the C=O groups. It was considered that C=O also had an activation effect on peroxide,[30] and it was speculated whether C=O groups were one of the active sites contributing to ROS generation. The N 1s spectrum of Co/NC@mSiO$_2$ (Figure 2j) showed characteristic peaks of pyridinic N (or Co−N), pyrrolic N, graphitic N, and N-oxide centered at 399.1, 400.4, 401.6, and 403.0 eV, respectively.[31] In contrast, no signals for the N element were detected in Co/mSiO$_2$, further indicating that the presence of CTAB had an important impact on the formation of NC dots. The obvious changes in the C 1s and N 1s spectra proved the improved electronic structures of Co/NC@mSiO$_2$ due to the SMSI effect.

Based on the characterization results, the Co clusters were successfully prepared via a double physical−chemical confinement strategy, and the SMSI effect between Co clusters and mSiO$_2$ containing NC dots improved the electronic structures.

Catalytic Oxidation of Organic Pollutants

The prepared catalysts were used to activate PMS for the degradation of various organic pollutants in an environment. Gaseous chlorobenzene, as one of typical and toxic chlorinated volatile organic compounds (VOCs), was first degraded in the

continuous flow system (Figure S9). For comparison, the chlorobenzene adsorption of Co/NC@mSiO$_2$ and Co/mSiO$_2$ samples quickly reached equilibrium within 120 min (Figure S10). Compared with the adsorption of gaseous chlorobenzene in pure water, the removal rate of chlorobenzene by Co/NC@mSiO$_2$ (∼8.0%) and Co/mSiO$_2$ (∼7.0%) samples was relatively high, while the mineralization rate was close to zero. After adding PMS, chlorobenzene removal efficiency was only 8.0% over mSiO$_2$ (Figure 3a,b). As for Co/mSiO$_2$ and commercial Co$_3$O$_4$, the removal and mineralization rates of chlorobenzene were about 30.0 and 6.5%, respectively. However, nearly 95.0% chlorobenzene was removed, and the highest mineralization rate reached 100.0% over Co/NC@mSiO$_2$. This suggested that Co/NC@mSiO$_2$ has a high activation activity for PMS and Co species was the main catalytic center. The mineralization rate gradually decreased with time, which may be caused by the consumption of PMS during the reaction. In the continuous flow system, chlorobenzene was continuously bubbled into the wet scrubber for reaction. As the reaction proceeded, PMS was gradually consumed and the generation of ROS was inhibited. Notably, the stable catalytic chlorobenzene oxidation was remained for a
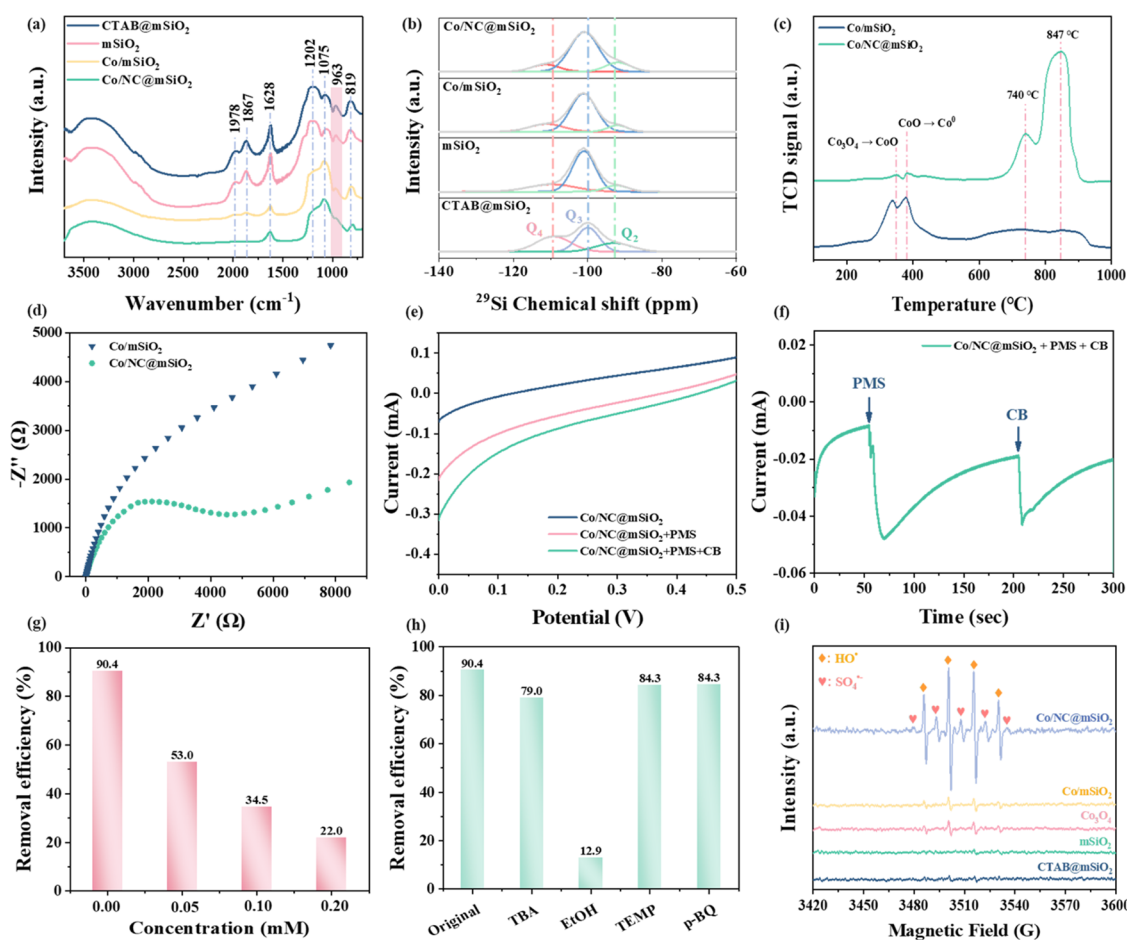
Figure 4. FTIR spectra (a), ^{29}Si solid-state NMR spectra (b) and H_2-TPR (c) of different samples. Nyquist plot curves of Co/mSiO$_2$ and Co/NC@mSiO$_2$ (d). Linear sweep voltammetry (LSV) curves of Co/NC@mSiO$_2$ under various conditions (e). Current response after the addition of PMS and chlorobenzene (f). Effect of AgNO$_3$ on chlorobenzene degradation by Co/NC@mSiO$_2$ (g). Effect of various radical scavengers on chlorobenzene degradation by Co/NC@mSiO$_2$ (h). Electron paramagnetic resonance (EPR) spectra of HO$^\bullet$ and SO$_4^{\bullet-}$ (i). ([Chlorobenzene]$_o$ = 30 ppmv, [Catalyst]$_o$ = 50 mg L^{-1}, [PMS]$_o$ = 16 mM, [AgNO$_3$]$_o$ = 0.05−0.20 mM, [TBA]$_o$ = 20 mM, [EtOH]$_o$ = 20 mM, [TEMP]$_o$ = 0.05 mM, [p-BQ]$_o$ = 0.05 mM, T = 25 °C).

much longer time and the mineralization rate gradually increased with time when PMS was intermittently added (Figure S11). Compared with Co/mSiO$_2$, Co/NC@mSiO$_2$ exhibited a superior catalytic performance due to the confined Co clusters in mSiO$_2$ containing NC dots.

The pH value of wastewater is generally variable in different industrial processes. For example, the pH value of the wastewater discharged from the steel industry fluctuates between 4 and 12,[32] while it is generally changed from 1.5 to 6 in the mine wastewater.[33] Therefore, it is necessary to keep high catalytic stability in a wide pH range for industrial application. Figure 3c shows that Co/NC@mSiO$_2$ was kept extremely effective for PMS activation in the wide pH range of 2−11, with about 90.0% chlorobenzene removal efficiency. This was far superior to the reported transition-metal-based peroxide activation system, which usually maintained catalytic activity in the narrow pH range of 5−9 (Table S6). The double-confinement and SMSI effects not only achieved the superior activity of Co clusters but also boosted their stability. This, on the one hand, prevented the catalytic sites on the catalyst from deactivation under strong acidic conditions. On the other hand, the acidic Si−OH groups of the Co/NC@mSiO$_2$ surface possibly neutralized partial hydroxide ions to avoid the quenching of radicals even in strong alkaline

conditions. Therefore, Co/NC@mSiO$_2$ successfully broke through the pH limitation and can cope with pollutant removal even in extremely acidic and alkaline environments. Compared with other works (Table S6), the Co ion leaching of Co/NC@mSiO$_2$ after reaction was only 0.11 mg L^{-1} (Figure 3d), which met with the surface water concentration limit of 1 mg L^{-1} in China (GB 3838-2002). This was also closely associated with the protection of the confined nanospaces. The XRD pattern (Figure S12) of the used Co/NC@mSiO$_2$ was similar to the fresh one, indicating that the Co clusters equipped with outstanding stability and did not gather to generate big NPs during the catalytic reaction. This was attributed to the unique SMSI effect and abundant mesopores, both of which prevented the aggregation of Co clusters and enabled excellent stability for pollutant degradation under very harsh environments.

Besides superior chlorobenzene removal, the Co/NC@mSiO$_2$/PMS system also exhibited excellent catalytic oxidation performance for other aromatic VOC waste gas. The highest removal rates of styrene and toluene were up to 98.0 and 91.0%, respectively (Figure 3e). In addition, Co/NC@mSiO$_2$ showed outstanding catalytic degradation performances toward the refractory organic pollutants in wastewater, such as 2-chlorophenol (2-CP), 2,4-dichlorophenol (2,4-DCP), and

2,4,6-trichlorophenol (2,4,6-TCP) from the medicine, pesticides, and dye industries, respectively; norfloxacin (NOR), a representative of antibiotics; bisphenol A (BPA), a pervasive endocrine disruptor; and rhodamine B (RhB) and methylene blue (MB), the widely used organic dyes. All organic pollutants were quickly degraded within 20 min with an exceptional k_{obs} value (Figure 3f−g). In particular, RhB and 2,4-DCP were fast and completely degraded within 10 s (Figures S13 and S14). These results strongly demonstrated that Co/NC@mSiO$_2$ had an exceptional activity and wide applicability for degradation of various organic contaminants in an environment.

Pollutant Oxidation Mechanism over Co/NC@mSiO$_2$

Co/NC@mSiO$_2$ exhibited dramatic superiorities in the catalytic oxidation of organic pollutants, while the reasons were still unclear. It is well known that the SMSI effect can greatly contribute to the excellent performance by tuning the electronic structures and improving the stability of catalysts.[18] Several characterizations were then conducted to explore the SMSI effect over the Co-based catalysts. In Figure 4a, the FTIR spectra of the prepared catalysts displayed two absorption peaks at 3557 and 1628 cm^{-1}, corresponding to the stretching and bending vibrations of hydroxyl (−OH), respectively. Compared with Co/mSiO$_2$, the peak at 963 cm^{-1} derived from the bending vibration of Si−OH disappeared over Co/NC@mSiO$_2$, illustrating the total consumption of Si−OH groups.[34] The bands at 1075 and 819 cm^{-1} attributed to the stretching vibration of Si−O−Si bonds, and the other three bands at 1978, 1867, and 1628 cm^{-1} ascribed to the overtones and combination of intense Si−O fundamental modes were also greatly weakened.[35] This indicated that CTAB@mSiO$_2$ as the support provided abundant Si−OH groups to anchor Co clusters. The ^{29}Si magic-angle spinning (MAS)−NMR spectra of the catalysts further verified this hypothesis (Figure 4b and Table S7). All of the samples showed three chemical shifts centered on −93 (Q^2), −100 (Q^3), and −109 (Q^4) ppm, corresponding to Si(OSi)$_2$(OH)$_2$, Si(OSi)$_3$OH, and Si(OSi)$_4$,[36] respectively. The Q^3 content of Co/NC@mSiO$_2$ was much higher than that of Co/mSiO$_2$, suggesting that the metal siloxane bridge conjecture could be well supported. The decrease of $Q^4/(Q^2 + Q^3)$ was considered as an evidence of the Co insertion since it caused steric constraints and difficult condensation in the mSiO$_2$ shell.[37] In addition, the H$_2$-TPR spectra of Co/NC@mSiO$_2$ (Figure 4c) showed a poor low-temperature reduction region at 349 °C attributed to the reduction of Co$_3$O$_4$ to CoO and the second region at 382 °C associated with the subsequent reduction of CoO to Co^0. Interestingly, two strong and broad reduction peaks around 740 and 847 °C were observed, which were caused by the reduction of Co clusters strongly interacting with the surface Si−OH groups.[38] However, Co/mSiO$_2$ showed the broader reduction peaks at low temperatures of 200−500 °C, indicating the weak interactions between Co NPs and mSiO$_2$. Consequently, it can be concluded that the abundant Si−OH groups provided by CTAB@mSiO$_2$ as well as the NC dots can simultaneously act as anchor sites for Co clusters. These two together facilitated the SMSI effect between Co clusters and mSiO$_2$ containing NC dots, which thus improved the electron transport properties of Co/NC@mSiO$_2$ and was beneficial for PMS activation.

Additionally, the electrochemical tests were also performed to investigate the electronic structures of Co/NC@mSiO$_2$ due to the enhanced SMSI effect. Compared with Co/mSiO$_2$, Co/

NC@mSiO$_2$ showed a much smaller semicircle at the high-frequency regions of the Nyquist plots (Figure 4d), verifying its quite higher surface charge. The stronger electron transfer capability of Co/NC@mSiO$_2$ was also proved by the cyclic voltammetry (CV) curves (Figure S15). In Figure 4e, linear sweep voltammetry (LSV) exhibited a noticeably increased current over the Co/NC@mSiO$_2$ electrode upon the addition of PMS and chlorobenzene. Similarly, the chronoamperometry curves also showed a sharp drop in current density after the addition of PMS (Figure 4f), displaying the strong electron transfer between PMS and Co/NC@mSiO$_2$ to form a metastable reactive complex.[39] The further addition of chlorobenzene to the solution caused an increased current since the Co species directly mediated electron transfer between chlorobenzene and PMS. When AgNO$_3$ as the electron scavenger was added into the Co/NC@mSiO$_2$/PMS system, it was found that the chlorobenzene removal greatly dropped to 22.0% (Figure 4g). This further indicated that the electron transfer played an important role in chlorobenzene degradation. Furthermore, the XPS spectra of Co/NC@mSiO$_2$ after reaction was analyzed (Figure S16 and Table S8). The fitting peak positions were obviously shifted in both C 1s and N 1s spectra of Co/NC@mSiO$_2$ after reaction. The relative intensity of the C=O bond for the used Co/NC@mSiO$_2$ was slightly increased compared to that of the fresh one, excluding the effect of C=O groups on PMS activation. For the Co 2p spectrum of Co/NC@mSiO$_2$, the Co^{2+} contents were slightly reduced from 73.6 to 68.9% due to the efficient Co^{2+}/Co^{3+} cycles, further indicating that Co species was the active sites for PMS activation. All of these results demonstrated the strong electron transfer between chlorobenzene and PMS over Co/NC@mSiO$_2$.

To identify the radicals generated from PMS activation by Co/NC@mSiO$_2$, the ROS-trapping experiments were conducted during chlorobenzene degradation. Ethanol (EtOH) was chosen as the scavenger for both HO$^\bullet$ and SO$_4^{\bullet-}$, tert-butyl alcohol (TBA) for HO$^\bullet$, p-BQ for superoxide radicals (O$_2^{\bullet-}$), and TEMP for single oxygen (^{1}O$_2$). As shown in Figure 4h, only a weak decrease of chlorobenzene removal efficiency occurred in the Co/NC@mSiO$_2$/PMS system when TBA was added. In contrast, it was sharply decreased from 90.4 to 12.9% upon the addition of EtOH, indicating that SO$_4^{\bullet-}$ played a dominant role in chlorobenzene degradation. The addition of TEMP and p-BQ did not significantly inhibit the chlorobenzene degradation, suggesting that ^{1}O$_2$ or O$_2^{\bullet-}$ was not involved in the reaction process. The EPR technique was employed to detect ROS generated from PMS activation. As seen in Figure 4i, no obvious EPR signal was detected in both CATB@mSiO$_2$ and mSiO$_2$ solution with DMPO as the spin-trapping agent, indicating that they cannot efficiently activate PMS for radical generation. As expected, Co/NC@mSiO$_2$ exhibited the strong characteristic peaks of DMPO-HO$^\bullet$ and DMPO-SO$_4^{\bullet-}$ adducts. The fast transformation of DMPO-SO$_4^{\bullet-}$ to DMPO-HO$^\bullet$ led to the higher signal intensity of HO$^\bullet$. However, for Co$_3$O$_4$ and Co/mSiO$_2$, very poor characteristic peaks of DMPO-HO$^\bullet$ and DMPO-SO$_4^{\bullet-}$ adducts were detected. No signals of ^{1}O$_2$ (Figure S17) and O$_2^{\bullet-}$ (Figure S18) could be observed over the Co-based catalysts, proving that PMS was reduced by the radical pathway after Co loading. The strong interaction between positively charged Co and negatively charged O in HSO$_5^-$ caused PMS dissociation into HO$^\bullet$ and SO$_4^{\bullet-}$.[40] The EPR signal intensity of Co/NC@mSiO$_2$ was much stronger than that of Co/mSiO$_2$,
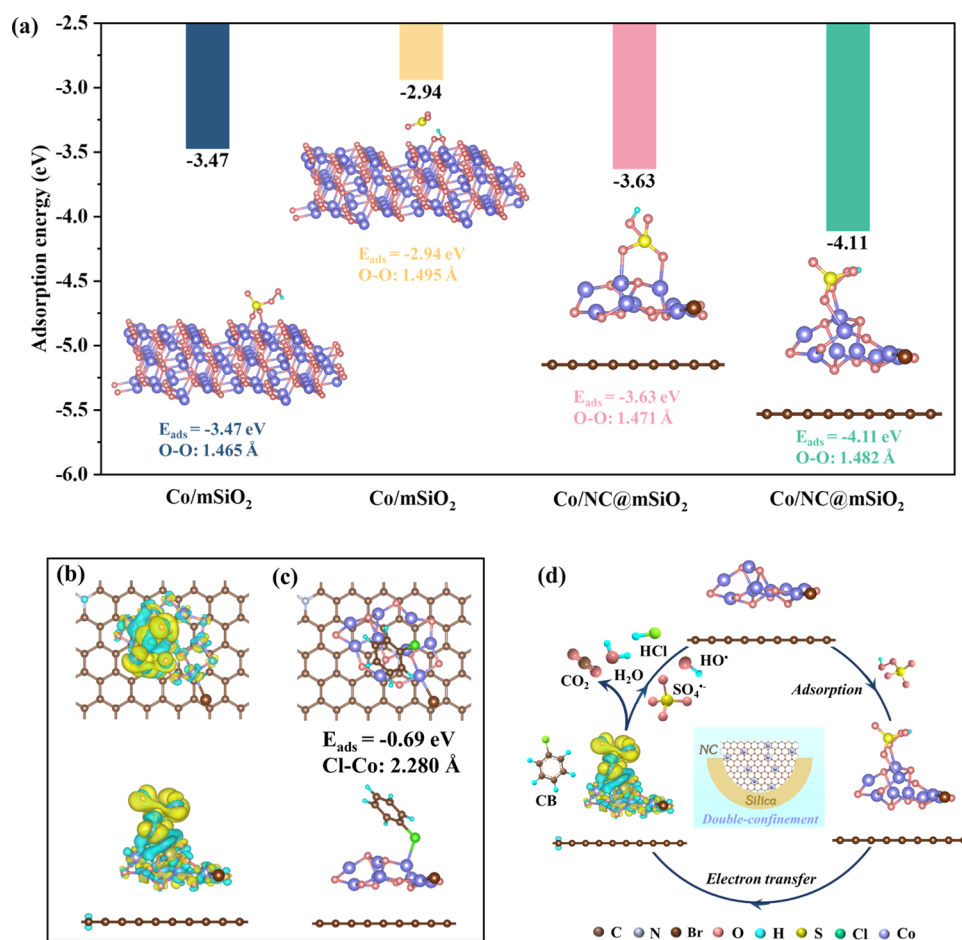
Figure 5. Adsorption configurations of PMS on Co/mSiO$_2$ and Co/NC@mSiO$_2$ through coordinating with S-adjacent (type I) and H-adjacent (type II) O atoms in the peroxide bond, respectively (a). Charge density of PMS on Co/NC@mSiO$_2$ through type II adsorption configurations (b). Adsorption configurations of chlorobenzene on Co/NC@mSiO$_2$ (c). Proposed reaction mechanism for chlorobenzene oxidation by Co/NC@mSiO$_2$ (d).

which was well consistent with their catalytic performance of gaseous VOC degradation. The radical reaction occurring in confined nanospaces finally increased the exposure of radicals to pollutants and avoided self-quenching in the bulk aqueous phase via the confinement effect.[8] Thus, the double-confined Co/NC@mSiO$_2$ dramatically improved the catalytic activity for pollutant degradation.

Density functional theory (DFT) calculations were performed to gain insight into the effect of NC dots on the catalytic activity of the catalysts. The optimized models of Co/NC@mSiO$_2$ (Figure S19) and Co/mSiO$_2$ (Figure S20) were proposed according to the previous XAFS and XPS results. Generally, PMS activation on the surface of catalysts consisted of two continuous steps: the adsorption toward O sites of PMS and then activation for ROS production.[31] First, we examined the adsorption of PMS on the catalyst surface. Two possible adsorption configurations were considered: coordinating the Co atom with the O atom adjacent to the S atom (dangling O1, type I adsorption) of the peroxide bond (O—O) and the O atom adjacent to the H atom (O2 of —OOH, type II adsorption). As seen in Figure 5a, the dangling O1 of PMS was stably adsorbed on the Co site of the Co$_3$O$_4$(311) surface, with an adsorption energy of −3.47 eV and O—O bond length of 1.465 Å. However, the O2 of PMS cannot be stably adsorbed on the Co$_3$O$_4$(311) surface. The O2 and S in PMS were almost unbonded, indicating that the type II adsorption of

PMS in Co/mSiO$_2$ did not exist. However, for Co/NC@mSiO$_2$, both O1 and O2 in PMS could be stably adsorbed on the Co site of the Co$_9$O$_{10}$ cluster encapsulated in NC dots, with an adsorption energy of −3.63 and −4.11 eV, respectively. In addition, the O—O bond length of PMS in type I and II adsorption configurations was elongated to 1.471 and 1.482 Å, respectively. This indicated that the existence of NC dots in Co/NC@mSiO$_2$ can greatly lower the adsorption energy barrier of PMS molecules onto the catalysts compared with Co/mSiO$_2$. Additionally, a strong charge transfer from Co/NC@mSiO$_2$ to PMS occurred via type II adsorption configuration, enabling spontaneous dissociation of the O—O bond into HO$^\bullet$ and SO$_4^{\bullet-}$ radicals (Figure 5b). In contrast to Co/NC@mSiO$_2$, the charge transfer was weak from Co/mSiO$_2$ to PMS, according to the charge density in Figure S21a, which well agreed with the electrochemical results. Furthermore, chlorobenzene showed a higher adsorption energy (−0.69 eV) and shorter Cl—Co bond length (2.280 Å) in Co/NC@mSiO$_2$ (Figure 5c) than those in Co/mSiO$_2$ (Figure S21b). This indicated that chlorobenzene was much easier to be adsorbed and oxidized in the Co/NC@mSiO$_2$/PMS system. The double-confinement and SMSI effects over Co/NC@mSiO$_2$ tremendously promoted reactant adsorption and electron transfer, leading to the efficient chlorobenzene degradation.

The analysis results in Figure S22a showed that, compared with liquid intermediates, relatively few intermediates were detected in the outlet gas with a very low concentration, which effectively solved the secondary pollution problem caused by byproduct emission in the gas–solid catalytic reaction. The generated intermediates in liquid phase mainly included ketonene (m/z 43.0106), acetaldehyde (m/z 45.0262), formic acid (m/z 47.0055), methyl peroxide (m/z 49.0211), methyl chloride (m/z 50.9923), acetone (m/z 59.0419), acetic acid (m/z 61.0211), butylaldehyde (m/z 73.0575), hydroxyl acetate (m/z 77.0524), furan, 2-methyl (m/z 83.0419), 2-propionic acid, methyl ester (m/z 85.0211), butane, 1-chloro- (m/z 93.0393), phenol (m/z 95.0419), ethanol, 2,2-dichloro- (m/z 114.9640), etc., implying the serious destruction of chlorobenzene (Figure S22b–d and Table S9). In the Co/NC@mSiO$_2$/PMS system, the highly selective SO$_4^{\bullet-}$ attacked chlorobenzene to form a carbon-positive radical through electron capture or HO$^\bullet$ attacked chlorobenzene to form chlorophenol through a substitution reaction. Subsequently, benzoquinones were formed via the ketonylation reaction and finally attacked by HO$^\bullet$ for the ring-opening reaction. Finally, the small molecular intermediates were further attacked by radicals to mineralize into CO$_2$, HCl, and H$_2$O.

Through above analysis, the excellent PMS activation performance over Co/NC@mSiO$_2$ is summarized in Figure 5d. The O2 of −OOH in a PMS molecule was first adsorbed on the Co site of the Co$_9$O$_{10}$ cluster encapsulated in NC dots, and then a strong electron transfer occurred from Co/NC@mSiO$_2$ to PMS. Consequently, HO$^\bullet$ and SO$_4^{\bullet-}$ radicals were abundantly generated to oxidize the pollutant molecules. The double-confined Co/NC@mSiO$_2$ greatly promoted PMS activation into radicals via electron transfer and finally achieved efficient organic pollutant degradation in AOPs.

■ CONCLUSIONS

In summary, we originally developed the double-confined Co clusters in mSiO$_2$ containing NC dots by a facile and green solvent-free method. The double physical–chemical confinement strategy well cooperated in preventing metal aggregation and enhancing the SMSI effect for optimizing electronic structures. The obtained Co/NC@mSiO$_2$ exhibited exceptional PMS activation capability for removal of various organic pollutants. Additionally, it kept unprecedented catalytic activity and stability in a very wide pH range (from 2 to 11) with extremely low Co ion leaching due to the SMSI effect between Co clusters and mSiO$_2$ containing NC dots. Co/NC@mSiO$_2$ possessed strong PMS adsorption and charge transfer, enabling the efficient O−O bond dissociation of PMS into HO$^\bullet$ and SO$_4^{\bullet-}$ radicals. This work represents a novel double-confinement strategy for the design of the highly active and stable catalysts and paves the way for industrial application of AOPs in environmental remediation.

■ EXPERIMENTAL SECTION

Catalyst Synthesis

The mesoporous silica was prepared by a typical sol−gel method. First, 3 mL of NH$_3$·H$_2$O was added to a stirred solution of ethanol (30 mL) and deionized water (100 mL). Then, 0.45 g of CTAB was dissolved in the above solution. After 30 min stirring, 3 mL of TEOS was subsequently added dropwise and vigorously stirred for 24 h at room temperature. Finally, the products were collected by centrifugation, washed with deionized water and ethanol several times, and dried at 60 °C for 12 h to obtain CTAB@mSiO$_2$. Pure

mSiO$_2$ was obtained by calcination of the CTAB@mSiO$_2$ in a furnace at 500 °C for 5 h in air.

The Co/NC@mSiO$_2$ catalyst was synthesized via a one-step calcination method. Typically, the CTAB@mSiO$_2$ (1.0 g) was mixed with Co(NO$_3$)$_2$·6H$_2$O (1.08 mmol) in an agate mortar, followed by manual grinding for 30 min. The theoretical Co load was 6 wt %. The fully mixed powder was then calcined at 500 °C for 5 h in air to obtain Co/NC@mSiO$_2$. In contrast, the Co/mSiO$_2$ sample with the same Co load was also prepared with identical procedures except that pristine mSiO$_2$ served as the support.

Catalyst Characterization

Scanning electron microscopy, transmission electron microscopy, high-resolution TEM, spherical aberration-corrected HAADF-STEM, X-ray diffraction, N$_2$ adsorption−desorption isotherms, H$_2$ temperature-programmed reduction (H$_2$-TPR), Raman spectroscopy, ^{29}Si magic-angle spinning (MAS) NMR, Fourier transform infrared (FTIR) spectroscopy, in situ thermogravimetry coupled with FTIR, X-ray photoelectron spectroscopy, electron paramagnetic resonance, X-ray absorption fine structure (XAFS) were used to characterize the physical and chemical performances of the prepared catalysts. The detailed characterization process is provided in the Supporting Information.

Catalytic Activity Evaluation

The VOC degradation was carried out in a wet scrubbing reactor with a working volume of 1 L (Figure S9).[41,42] The experimental system mainly consisted of a gas distribution system, a reaction system, and an analytic system. The bubbler was installed near the bottom of the wet scrubbing reactor to distribute the gas. The average diameters of microbubble were determined below 1 μm. In the continuous flow system, the flows and concentrations of VOC gas stream were regulated by mass flowmeters (MT-50-4J, Beijing HORIBA METRON Instruments Co., Ltd.). The total air stream was supplied continuously at a flow rate of 1 L min^{-1}. The mass flowmeters were simultaneously started to bubble the corresponding VOC solution. The concentrated VOC gas stream was transferred to a mixing bottle, where the air stream was fed to dilute the VOC-containing gas stream. Then, the diluted VOC gas stream entered the wet scrubber to initiate a gas−liquid reaction with the addition of the corresponding catalyst and PMS. Aromatic VOC mainly derives from the printing, coating, and pharmaceutical industries with characteristic low concentrations. Based on this, the initial concentration of VOC was set at 30 ppmv. A thermostatic water bath was used to maintain the reaction temperature so that the reaction was proceeded at a constant temperature (T = 25 °C).

The concentrations of VOC and CO$_2$ were continuously detected using a gas chromatograph (GC) (9790II, Fuli) with two flame-ionization detectors (FIDs). One FID equipped with an Rt-Q-BOND PLOT column (30 m × 0.25 mm id, film thickness 10 μm) was used for VOC analysis, and the other FID equipped with a packed column (TDX-01, 3 m × 3 mm) by a methane converter with a nickel catalyst was used to detect CO$_2$. Additionally, a proton transfer reaction−time of flight−mass spectrometer (PTR-ToF-MS, Ionicon Analytik GmbH, Innsbruck, Austria) was used to detect trace VOCs and the byproducts online.

The removal efficiency of VOCs was calculated by equations as follows:

$$\text{removal efficiency (\%)} = \frac{[\text{VOCs}]_{\text{inlet}} - [\text{VOCs}]_{\text{outlet}}}{[\text{VOCs}]_{\text{inlet}}} \times 100\%$$

(1)

$$\text{mineralization rate (\%)} = \frac{[\text{CO}_2]_{\text{outlet}}}{[\text{VOCs}]_{\text{inlet}} \times n} \times 100\%$$

(2)

where $[\text{VOCs}]_{\text{inlet}}$ and $[\text{VOCs}]_{\text{outlet}}$ represent the concentrations of gas VOCs at the inlet and outlet, respectively, ppmv; $[\text{CO}_2]_{\text{outlet}}$ represents the outlet CO$_2$ concentration, ppmv; and n represents the C atoms of the VOC molecule.

Batch degradation experiments were conducted in a 250 mL beaker at room temperature under magnetic stirring. PMS activation was performed with the mixed solution of pollutants (10 mg L^{-1}), PMS (0.32 mM), and catalyst (10 mg L^{-1}) in a constant temperature water bath at 25 °C. All of the degradation experiments were conducted in distilled water. As the reaction proceeded, the catalyst was added into the mixed solution for 30 min to achieve the absorption equilibrium, followed by adding PMS. Aliquots of the reaction solution (0.5 mL) were withdrawn using an injection syringe at designated time intervals for high-performance liquid chromatography (HPLC, Agilent 1260 Infinity II, Germany) analysis. Na$_2$SO$_3$ (5 mM, 0.5 mL) was added to quench the reaction. All of the samples were ready to be filtered through an organic phase filter (0.22 μm) before analysis. The mobile phase consisted of water (A) and methanol/acetonitrile (B) with an isocratic elution of A/B (v/v) at a flow rate of 1 mL min^{-1}.

The catalytic reaction kinetics were obtained using a fitted first-order reaction kinetics equation:

$$k_{\mathrm{obs}} = -\ln\left(\frac{C_t}{C_o}\right) \tag{3}$$

where C_o and C_t represent the initial and real-time concentrations of the pollutants, respectively, mg L^{-1} and k_{obs} is the rate constant of the fitted first-order kinetics.

DFT Computational Method

The adsorption energy (E_{ads}) of PMS and chlorobenzene and the activation mechanisms of PMS with two different models, including Co$_3$O$_4$(311) and Co$_9$O$_{10}$ clusters for Co/mSiO$_2$ and Co/NC@mSiO$_2$, were studied by density functional theory (DFT) calculations. The detailed calculation methods are provided in the Supporting Information.

■ ASSOCIATED CONTENT

⑤ⁱ Supporting Information

The Supporting Information is available free of charge at https://pubs.acs.org/doi/10.1021/jacsau.3c00147.

> Additional experimental details, characterization, catalytic activity results, computational methods, and additional data (PDF)

■ AUTHOR INFORMATION

Corresponding Author

Haibao Huang − *School of Environmental Science and Engineering, Sun Yat-Sen University, Guangzhou 510000, P. R. China;* ⓞ orcid.org/0000-0002-9259-7179; Email: seabao8@gmail.com

Authors

Xiaowen Xie − *School of Environmental Science and Engineering, Sun Yat-Sen University, Guangzhou 510000, P. R. China*

Mingshan Zhu − *Guangdong Key Laboratory of Environmental Pollution and Health, School of Environment, Jinan University, Guangzhou 510000, P. R. China;* ⓞ orcid.org/0000-0002-5926-5383

Fei Xiao − *School of Environmental Science and Engineering, Sun Yat-Sen University, Guangzhou 510000, P. R. China*

Yongjie Xiang − *School of Environmental Science and Engineering, Sun Yat-Sen University, Guangzhou 510000, P. R. China*

Huanran Zhong − *School of Environmental Science and Engineering, Sun Yat-Sen University, Guangzhou 510000, P. R. China*

Zhimin Ao − *Advanced Interdisciplinary Institute of Environment and Ecology, Beijing Normal University, Zhuhai 519087, P. R. China;* ⓞ orcid.org/0000-0003-0333-3727

Complete contact information is available at:
https://pubs.acs.org/10.1021/jacsau.3c00147

Notes

The authors declare no competing financial interest.

■ ACKNOWLEDGMENTS

■ REFERENCES

(1) Guo, Z.; Li, C.; Gao, M.; Han, X.; Zhang, Y.; Zhang, W.; Li, W. Mn-O covalency governs the intrinsic activity of Co-Mn spinel oxides for boosted peroxymonosulfate activation. *Angew. Chem., Int. Ed.* **2021**, *60*, 274−280.

(2) Lee, J.; Gunten, U.; Kim, J.-H. Persulfate-based advanced oxidation: Critical assessment of opportunities and roadblocks. *Environ. Sci. Technol.* **2020**, *54*, 3064−3081.

(3) Liu, Y.; Liu, L.; Wang, Y. A Critical review on removal of gaseous pollutants using sulfate radical-based advanced oxidation technologies. *Environ. Sci. Technol.* **2021**, *55*, 9691−9710.

(4) Ma, Y.; Wang, H.; Lv, X.; Xiong, D.; Xie, H.; Zhang, Z. Three-dimensional ordered mesoporous Co$_3$O$_4$/peroxymonosulfate triggered nanoconfined heterogeneous catalysis for rapid removal of ranitidine in aqueous solution. *Chem. Eng. J.* **2022**, *443*, No. 136495.

(5) Zhang, Q.; Sun, X.; Dang, Y.; Zhu, J. J.; Zhao, Y.; Xu, X.; Zhou, Y. A novel electrochemically enhanced homogeneous PMS-heterogeneous CoFe$_2$O$_4$ synergistic catalysis for the efficient removal of levofloxacin. *J. Hazard. Mater.* **2022**, *424*, No. 127651.

(6) Shao, S.; Li, X.; Gong, Z.; Fan, B.; Hu, J.; Peng, J.; Lu, K.; Gao, S. A new insight into the mechanism in Fe$_3$O$_4$@CuO/PMS system with low oxidant dosage. *Chem. Eng. J.* **2022**, *438*, No. 135474.

(7) Shen, S.; Zhou, X.; Zhao, Q.; Jiang, W.; Wang, J.; He, L.; Ma, Y.; Yang, L.; Chen, Z. Understanding the nonradical activation of peroxymonosulfate by different crystallographic MnO$_2$: The pivotal role of Mn(III) content on the surface. *J. Hazard. Mater.* **2022**, *439*, No. 129613.

(8) Zhang, B.-T.; Yan, Z.; Liu, Y.; Chen, Z.; Zhang, Y.; Fan, M. Nanoconfinement in advanced oxidation processes. *Crit. Rev. Environ. Sci. Technol.* **2023**, *53*, 1197−1228.

(9) Li, X.; Huang, X.; Xi, S.; Miao, S.; Ding, J.; Cai, W.; Liu, S.; Yang, X.; Yang, H.; Gao, J.; Wang, J.; Huang, Y.; Zhang, T.; Liu, B. Single cobalt atoms anchored on porous N-doped graphene with dual reaction sites for efficient Fenton-like catalysis. *J. Am. Chem. Soc.* **2018**, *140*, 12469−12475.

(10) Chen, Y.; Ji, S.; Chen, C.; Peng, Q.; Wang, D.; Li, Y. Single-atom catalysts: Synthetic strategies and electrochemical applications. *Joule* **2018**, *2*, 1242−1264.

(11) Pu, Z.; Amiinu, I. S.; Cheng, R.; Wang, P.; Zhang, C.; Mu, S.; Zhao, W.; Su, F.; Zhang, G.; Liao, S.; Sun, S. Single-atom catalysts for electrochemical hydrogen evolution reaction: Recent advances and future perspectives. *Nano-Micro Lett.* **2020**, *12*, 21.

(12) Cheng, N.; Zhang, L.; Doyle-Davis, K.; Sun, X. Single-atom catalysts: From design to application. *Electrochem. Energy Rev.* **2019**, *2*, 539−573.

(13) Qian, J.; Gao, X.; Pan, B. Nanoconfinement-mediated water treatment: From fundamental to application. *Environ. Sci. Technol.* **2020**, *54*, 8509−8526.

(14) Wang, Z.; Shen, J.; Liu, J.; Xu, X.; Liu, Z.; Hu, R.; Yang, L.; Feng, Y.; Liu, J.; Shi, Z.; Ouyang, L.; Yu, Y.; Zhu, M. Self-supported and flexible sulfur cathode enabled via synergistic confinement for

high-energy-density lithium-sulfur batteries. *Adv. Mater.* **2019**, *31*, No. 1902228.

(15) Yin, Y.; Shi, L.; Li, W.; Li, X.; Wu, H.; Ao, Z.; Tian, W.; Liu, S.; Wang, S.; Sun, H. Boosting fenton-like reactions via single atom Fe catalysis. *Environ. Sci. Technol.* **2019**, *53*, 11391−11400.

(16) Lin, J.; Chen, S.; Xiao, H.; Zhang, J.; Lan, J.; Yan, B.; Zeng, H. Ultra-efficient and stable heterogeneous iron-based Fenton nano-catalysts for degrading organic dyes at neutral pH via a chelating effect under nanoconfinement. *Chem. Commun.* **2020**, *56*, 6571−6574.

(17) Yang, Z.; Qian, J.; Yu, A.; Pan, B. Singlet oxygen mediated iron-based Fenton-like catalysis under nanoconfinement. *Proc. Natl. Acad. Sci. U.S.A.* **2019**, *116*, 6659−6664.

(18) Hu, Q.; Han, Z.; Wang, X.; Li, G.; Wang, Z.; Huang, X.; Yang, H.; Ren, X.; Zhang, Q.; Liu, J.; He, C. Facile synthesis of sub-nanometric copper clusters by double confinement enables selective reduction of carbon dioxide to methane. *Angew. Chem., Int. Ed.* **2020**, *59*, 19054−19059.

(19) Qin, L.; Gan, J.; Niu, D.; Cao, Y.; Duan, X.; Qin, X.; Zhang, H.; Jiang, Z.; Jiang, Y.; Dai, S.; Li, Y.; Shi, J. Interfacial-confined coordination to single-atom nanotherapeutics. *Nat. Commun.* **2022**, *13*, No. 91.

(20) Polshettiwar, V.; Cha, D.; Zhang, X.; Basset, J. M. High-surface-area silica nanospheres (KCC-1) with a fibrous morphology. *Angew. Chem., Int. Ed.* **2010**, *49*, 9652−9656.

(21) Kim, T.-W.; Chung, P.-W.; Lin, V. S. Y. Facile synthesis of monodisperse spherical MCM-48 mesoporous silica nanoparticles with controlled particle size. *Chem. Mater.* **2010**, *22*, 5093−5104.

(22) Al Khudhair, A.; Bouchmella, K.; Andrei, R. D.; Mehdi, A.; Mutin, P. H.; Hulea, V. One-step non-hydrolytic sol-gel synthesis of mesoporous SiO_2-Al_2O_3-NiO catalysts for ethylene oligomerization. *Microporous Mesoporous Mater.* **2021**, *322*, No. 111165.

(23) Lan, F.; Zhang, H.; Zhao, C.; Shu, Y.; Guan, Q.; Li, W. Copper clusters encapsulated in carbonaceous mesoporous silica nanospheres for the valorization of biomass-derived molecules. *ACS Catal.* **2022**, *12*, 5711−5725.

(24) Yang, J. Y.; Yang, J.; Zhou, Y.; Lin, W. G.; Wang, H. J.; Zhu, J. H. Effective nitrosamines trap derived from the in situ carbonized mesoporous silica MCM-41. *J. Hazard. Mater.* **2010**, *176*, 602−608.

(25) Gao, X.; Zhang, H.; Guan, J.; Shi, D.; Wu, Q.; Chen, K. C.; Zhang, Y.; Feng, C.; Zhao, Y.; Jiao, Q.; Li, H. Pomegranate-like core-shell Ni-NSs@MSNSs as a high activity, good stability, rapid magnetic separation, and multiple recyclability nanocatalyst for DCPD hydrogenation. *ACS Omega* **2021**, *6*, 11570−11584.

(26) Osorio-Vargas, P.; Lick, I. D.; Sobrevía, F.; Correa-Muriel, D.; Menares, T.; Manrique, R.; Casella, M. L.; Arteaga-Pérez, L. E. Thermal behavior, reaction pathways and kinetic implications of using a Ni/SiO₂ catalyst for waste tire pyrolysis. *Waste Biomass Valorization* **2021**, *12*, 6465−6479.

(27) Yin, Y.; Wu, H.; Shi, L.; Zhang, J.; Xu, X.; Zhang, H.; Wang, S.; Sillanpääd, M.; Sun, H. Quasi single cobalt sites in nanopores for superior catalytic oxidation of organic pollutants. *Environ. Sci.: Nano* **2018**, *5*, 2842−2852.

(28) Su, G.; Yang, C.; Zhu, J. J. Fabrication of gold nanorods with tunable longitudinal surface plasmon resonance peaks by reductive dopamine. *Langmuir* **2015**, *31*, 817−823.

(29) Chu, C.; Yang, J.; Zhou, X.; Huang, D.; Qi, H.; Weon, S.; Li, J.; Elimelech, M.; Wang, A.; Kim, J. H. Cobalt single atoms on tetrapyridomacrocyclic support for efficient peroxymonosulfate activation. *Environ. Sci. Technol.* **2021**, *55*, 1242−1250.

(30) Wu, J.; Wang, J.; Liu, C.; Nie, C.; Wang, T.; Xie, X.; Cao, J.; Zhou, J.; Huang, H.; Li, D.; Wang, S.; Ao, Z. Removal of gaseous volatile organic compounds by a multiwalled carbon nanotubes/peroxymonosulfate wet scrubber. *Environ. Sci. Technol.* **2022**, *56*, 13996−14007.

(31) Yao, Y.; Wang, C.; Yan, X.; Zhang, H.; Xiao, C.; Qi, J.; Zhu, Z.; Zhou, Y.; Sun, X.; Duan, X.; Li, J. Rational regulation of Co-N-C coordination for high-efficiency generation of $^1O_2$ toward nearly 100% selective degradation of organic pollutants. *Environ. Sci. Technol.* **2022**, *56*, 8833−8843.

(32) Chand, S.; Paul, B.; Kumar, M. Short-term leaching study of heavy metals from LD slag of important steel industries in Eastern India. *J. Mater. Cycles Waste Manage.* **2017**, *19*, 851−862.

(33) Tony, M. A.; Lin, L. S. Iron recovery from acid mine drainage sludge as Fenton source for municipal wastewater treatment. *Int. J. Environ. Anal. Chem.* **2022**, *102*, 1245−1260.

(34) Zhang, H.; Ke, D.; Cheng, L.; Feng, X.; Hou, X.; Wang, J.; Li, Y.; Han, S. CoPt-Co hybrid supported on amino modified SiO_2 nanospheres as a high performance catalyst for hydrogen generation from ammonia borane. *Prog. Nat. Sci.: Mater. Int.* **2019**, *29*, 1−9.

(35) dos Santos, J.; Krug, C.; Rosa, M. B. d.; Stedile, F. C.; Dupont, J.; Forte, M. d. C. The effect of silica dehydroxylation temperature on the activity of SiO_2-supported zirconocene catalysts. *J. Mol. Catal. A: Chem.* **1999**, *139*, 199−207.

(36) Kunc, F.; Balhara, V.; Sun, Y.; Daroszewska, M.; Jakubek, Z. J.; Hill, M.; Brinkmann, A.; Johnston, L. J. Quantification of surface functional groups on silica nanoparticles: comparison of thermogravi-metric analysis and quantitative NMR. *Analyst* **2019**, *144*, 5589−5599.

(37) Li, S.; Wang, J.; Ye, Y.; Tang, Y.; Li, X.; Gu, F.; Li, L. Composite Si-O-metal network catalysts with uneven electron distribution: Enhanced activity and electron transfer for catalytic ozonation of carbamazepine. *Appl. Catal., B* **2020**, *263*, No. 118311.

(38) Bustamante, T. M.; Campos, C. H.; Fraga, M. A.; Fierro, J. L. G.; Pecchi, G. Promotional effect of palladium in Co-SiO₂ core@shell nanocatalysts for selective liquid phase hydrogenation of chloroni-troarenes. *J. Catal.* **2020**, *385*, 224−237.

(39) Zhong, Q.; Xu, C.; Liu, Y.; Ji, Q.; Xu, Z.; Sun, D.; Zhou, S.; Yang, B.; Dai, Y.; Qi, C.; Yang, S.; He, H.; Li, S.; Sun, C. Defect-engineered $FeSe_{2-x}$@C with porous architecture for enhanced peroxymonosulfate-based advanced oxidation processes. *Appl. Catal., B* **2022**, *309*, No. 121259.

(40) Mi, X.; Wang, P.; Xu, S.; Su, L.; Zhong, H.; Wang, H.; Li, Y.; Zhan, S. Almost 100% peroxymonosulfate conversion to singlet oxygen on single-atom CoN_{2+2} sites. *Angew. Chem., Int. Ed.* **2021**, *133*, 4638−4643.

(41) Xie, X.; Cao, J.; Xiang, Y.; Xie, R.; Suo, Z.; Ao, Z.; Yang, X.; Huang, H. Accelerated iron cycle inducing molecular oxygen activation for deep oxidation of aromatic VOCs in MoS_2 co-catalytic Fe^{3+}/PMS system. *Appl. Catal., B* **2022**, *309*, No. 121235.

(42) Xie, X.; Xie, R.; Suo, Z.; Huang, H.; Xing, M.; Lei, D. A highly dispersed Co-Fe bimetallic catalyst to activate peroxymonosulfate for VOCs degradation in wet scrubber. *Environ. Sci.: Nano* **2021**, *8*, 2976−2987.